ACCEPTED MANUSCRIPT

Diffusion bonding of steels with a homogeneous microstructure throughout the joint

This Accepted Manuscript (AM) is a PDF file of the manuscript accepted for publication after peer review, when applicable, but does not reflect post-acceptance improvements, or any corrections. Use of this AM is subject to the publisher's embargo period and AM terms of use. Under no circumstances may this AM be shared or distributed under a Creative Commons or other form of open access license, nor may it be reformatted or enhanced, whether by the Author or third parties. By using this AM (for example, by accessing or downloading) you agree to abide by Springer Nature's terms of use for AM versions of subscription articles: https://www.springernature.com/gp/open-research/policies/accepted-manuscript-terms

The Version of Record (VOR) of this article, as published and maintained by the publisher, is available online at: https://doi.org/10.1007/s10853-024-10343-x. The VOR is the version of the article after copy-editing and typesetting, and connected to open research data, open protocols, and open code where available. Any supplementary information can be found on the journal website, connected to the VOR.

For research integrity purposes it is best practice to cite the published Version of Record (VOR), where available (for example, see ICMJE's guidelines on overlapping publications). Where users do not have access to the VOR, any citation must clearly indicate that the reference is to an Accepted Manuscript (AM) version.

Accepted manuscript

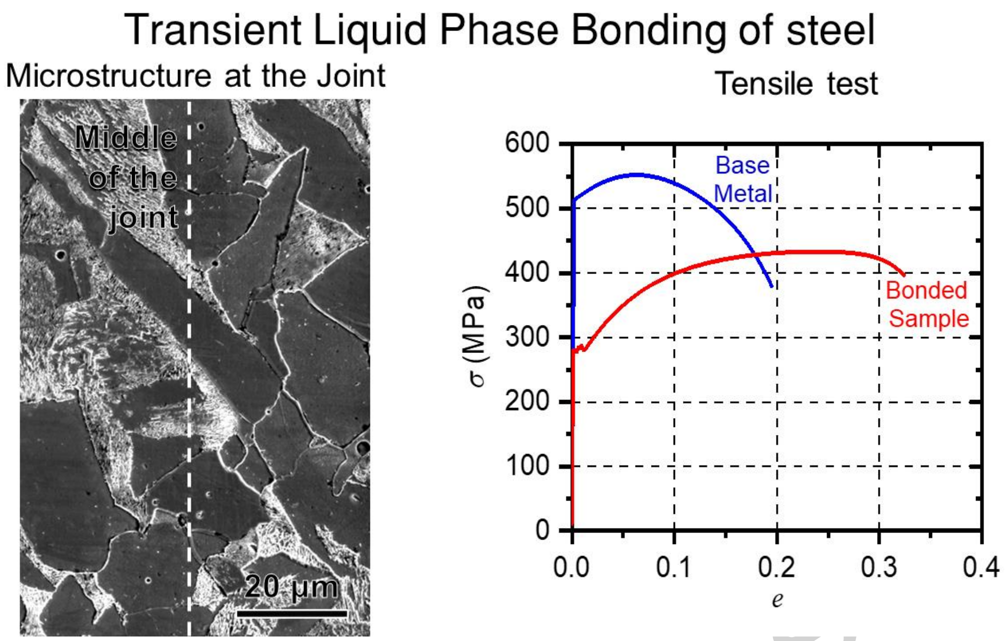

Diffusion bonding of steels with a homogeneous microstructure throughout the joint

Nicolás Di Luozzo [a,*], Michael Schulz [b], Michel Boudard [c], Silvina Limandri [d], Gastón Garbarino [e], Marcelo Fontana [a]

[a] Laboratorio de Sólidos Amorfos, INTECIN, Facultad de Ingeniería (UBA-CONICET), Paseo Colón 850, C1063ACV Buenos Aires, Argentina

[b] Heinz Maier-Leibnitz Zentrum, Technische Universität München, Lichtenbergstr. 1, 85748, Garching, Germany

[c] Université Grenoble Alpes, CNRS, Grenoble INP, LMGP, F-38000 Grenoble, France

[d] Instituto de Física Enrique Gaviola, (UNC-CONICET), Medina Allende s/n, Ciudad Universitaria, 5000 Córdoba, Argentina

[e] European Synchrotron Radiation Facility, 71 Avenue des Martyrs, CS 40220, Grenoble 38043, France

[*] Corresponding author

e-mail address: ndiluozzo@fi.uba.ar (N. Di Luozzo).

Abstract

Cold-finished carbon steel bars were bonded by means of the transient liquid phase bonding (TLPB) process using amorphous metallic foils of the eutectic Fe-B composition as filler material. A homogeneous microstructure throughout the joint was obtained. Traces of borides in the middle of the joint were the only distinguishable microconstituent from the base metal due to the TLPB process.

The B concentration profile across the joint was measured by neutron radiography and was found to be composed of a central sharp peak with a maximum concentration of 15.9 ppm B superimposed over a broad peak (base width of ≈ 5 mm) with a maximum concentration of 13.3 ppm B. Owing to this low range of B concentrations, boride precipitation was almost suppressed, and only a scarce number of borides were observed at the joint.

The resulting boride structure was identified as $Fe_{23}B_6$ by synchrotron microfocused X-ray diffraction, and its stabilization at room temperature is discussed.

The bonded samples were subjected to a bend test, with a bending angle of 180°, and no cracks were observed. In tension tests, the bonded samples attained an ultimate tensile strength (UTS) of 434 MPa, an elongation of 32.3% and a reduction area *q* of 51.2% - 78.6%, 165.6% and 75.4%, respectively, of the base metal. The fracture of the bonded samples occurred at the joint. It was determined that the decrease in UTS compared with that of the base metal was due to the recovery, recrystallization and grain growth

that occurred during the TLPB thermal cycle. In addition, from fracture surface observation, it was found that the decrease in q in bonded samples was caused by the presence of traces of borides at the joint, which were the result of the liquid phase that solidified during the cooling stage.

Keywords

Transient liquid phase bonding

Steels

Metallic glasses

Synchrotron microfocused X-ray diffraction

Neutron radiography

1. Introduction

Brazing is a widespread bonding technique for metallic, ceramic, composite and dissimilar base materials [1]. The base materials are bonded by heating them to the process temperature T_P in the presence of a filler material. T_P is above the *liquidus* temperature of the filler material and below the *solidus* temperature of the base material. Therefore, only the filler material melts, and its solidification during cooling from T_P produces the joint [1]. Brazing filler materials are supplied in the form of powders, pastes, tapes and foils.

Brazing foils of amorphous metallic glasses (AMGs) are typically produced by melt spinning [2] for brazing of metallic base materials - from now on, the base metal. However, the mechanical properties of the brazed joints are well below those of the base metal. This is due to the chemical composition of AMGs, which may contain B, Si and P - from now on, the solutes. As a result, the formation of intermetallic compounds, such as borides [3], silicides [4] and phosphides [5], occurs during cooling.

To address this problem, the transient liquid phase bonding (TLPB) was developed [6]. It promotes solute diffusion into the base metal by holding T_P for a prescribed time t_h to reduce solute concentration of the liquid phase between the bonding surfaces [7]. Indeed, strong, ductile, intermetallic-free joints were obtained by TLPB using foils of Ni-based AMGs alloyed with B and Si as filler material and carbon [8] and low-alloy steels [9] as base metal. However, an abrupt microstructural change was observed between the joint and the neighbouring base metal, which was due to the joint enrichment with Ni - a strong austenite stabilizer [10] - from the filler material.

---

[1] The joint is the region where the microstructure and/or the chemical composition differs from that of the base metal.

The same phenomena were observed in TLP-bonded carbon [11] and low-alloy steels [12] using foils of Fe-based B- and Si-alloyed AMGs as filler material. The joint enriched with Si exhibited an intermetallic-free fully ferritic microstructure, since Si is a ferrite-forming element [13], which clearly contrasts with the base metal.

This steep gradient in microstructure - and consequently in mechanical properties - leads to an inhomogeneous joint. However, adjusting both the chemical composition of the AMG and the TLPB thermal cycle to enable acceptable mass diffusion of solutes into the base metal can reduce or suppress this microstructure gradient.

AMGs of the binary Fe-B system at its deep eutectic were extensively investigated [14]. Despite it does not have the same glass-forming ability of brazing AMGs, B is the only solute of this filler material. Regarding its effects on steel, B is added to enhance its hardenability [15]. Therefore, its influence on the steel microstructure can be suppressed by avoiding high cooling rates, e.g., cooling in still air. In addition, small amounts of B, on the order of 8 to 50 ppm [16], must be added to avoid the precipitation of borides, which usually occurs at prior austenite grain boundaries (PAGBs).

Amorphous metallic foils composed of eutectic Fe-B were used to study the effect of applied pressure p in TLP-bonded low-carbon steel tubes [17]. However, neither the structure of borides nor the mechanical properties of the joint were determined.

In this context, detecting B is necessary. This can be done in ferrous alloys by neutron radiography (NR) and tomography, which proved to be successful in TLP-bonded steel tubes using foils of Fe-base B- and Si-alloyed AMG [18]. In addition, the mean linear attenuation coefficient $\bar{\mu}$ of B in steel for the given neutron energy spectrum was determined.

In this work, with the aim of obtaining a joint with a homogeneous microstructure, amorphous metallic foils composed of eutectic Fe-B were used for TLPB of carbon steel bars as base metal. A complete microstructure characterization was performed throughout the joint, which revealed a predominantly homogeneous microstructure. The structure of the scarce number of borides found at the joint was determined by synchrotron microfocused X-ray microdiffraction. Concerning solute distribution, the B concentration profile across the joint was measured by NR. In addition, both the strength and ductility of the bonded samples were compared with those of the base metal by tensile and bend tests.

2. Materials and Methods

The TLPB process was applied to join cold-finished carbon steel bars ASTM A108 1008 [19], whose composition is given in Table 1. The steel bars had a diameter of 25 mm. Amorphous metallic foils with the eutectic Fe-B composition ($Fe_{96.19}B_{3.81}$ wt.% ($Fe_{83}B_{17}$ at.%), thickness of 25 μm) were used as filler material.

Table 1

Chemical composition of the base metal in wt.% (at.%).

C	Mn	Si	S	P	Cr	Ni
0.107 (0.515)	1.090 (1.148)	0.240 (0.494)	0.0177 (0.0319)	0.0278 (0.0519)	0.0124 (0.0138)	0.0068 (0.0067)
Al	**Cu**	**V**	**Ca**	**Zn**	**B**	
0.0033 (0.0071)	0.0517 (0.0471)	0.0007 (0.0007)	0.0002 (0.0002)	0.0056 (0.0050)	-	

The thermal cycle of the TLPB process consisted of heating the bonding surfaces of the bars in contact with the filler material to T_P = 1300 °C, holding this temperature for t_h = 7 min and finally cooling the joint to room temperature. During the thermal cycle, a pressure p = 5 MPa was applied to the bars in the axial direction. The bonding process was carried out in an inert Ar atmosphere. For further details regarding the TLPB process and sample preparation, see reference [20].

2.1 Microstructure characterization

To characterize the morphology of the phases and to determine the microconstituents at the joint, scanning electron microscopy (SEM) was used. To this end, the samples were included in conductive compression mounting resin. Afterwards, the samples were polished with grinding papers (#100, #220, #400, #600 and #1200), diamond pastes (6 µm and 1 µm) and alumina suspensions (0.3 µm and 0.05 µm). For electron backscatter diffraction (EBSD) acquisition, the samples were finally subjected to vibratory polishing with colloidal silica (0.05 µm) for 10 h.

Secondary electron images were acquired via field emission (FE) SEM (FEI Quanta 250, ZEISS GeminiSEM 360) under standard operating conditions. EBSD maps were obtained using FE-SEM (ZEISS Sigma, equipped with a Schottky electron gun). For the acquisition, AZtec software was used to control the NordlysNano detector (Oxford Instruments), which was equipped with a CCD camera (1344×1024 pixels) and a 40 mm x 35 mm front phosphor screen. The SEM parameters used for EBSD map acquisition were 20 keV incident energy, 60 µm aperture, 8.5 mm working distance and 70° tilt angle. 8×8 binning was used for the CCD camera.

To achieve a reliable indexing of the non-indexed points of Fe-BCC phase without affecting the non-indexed areas associated with particles, initial postprocessing was performed to reindex the non-indexed points. In this postprocess, the non-indexed points exhibiting:

- A band contrast greater than 25
- At least one indexed Fe-BCC phase first neighbour

were reindexed as Fe-BCC phase, with an orientation given by the average of the orientations of their neighbours. Afterwards, the MTEX toolbox fill routine was used to fill missing data in the orientation maps [21]. Following this cleaning routine, maps were further analysed using AZtecCrystal software.

Quantitative chemical composition profiles of Mn and Si across the joint were obtained via electron probe microanalysis (EPMA) (JEOL JXA 8230). To this end, square bar specimens (8x8 mm^2) were cut from the core of the TLP-bonded bars by means of wire electrical discharge machining (WEDM), as shown in Fig. 1.

Quantitative point and zone measurements - in addition to qualitative maps of elements - were carried out by Energy-dispersive X-ray spectroscopy (EDS). These measurements were performed in a JEOL JSM-6510LV SEM - in backscattered mode, which was equipped with an Oxford X-MaxN 50 EDS with a 50 mm^2 detector.

The sample preparation for chemical composition characterization was the same as that for microstructure analysis.

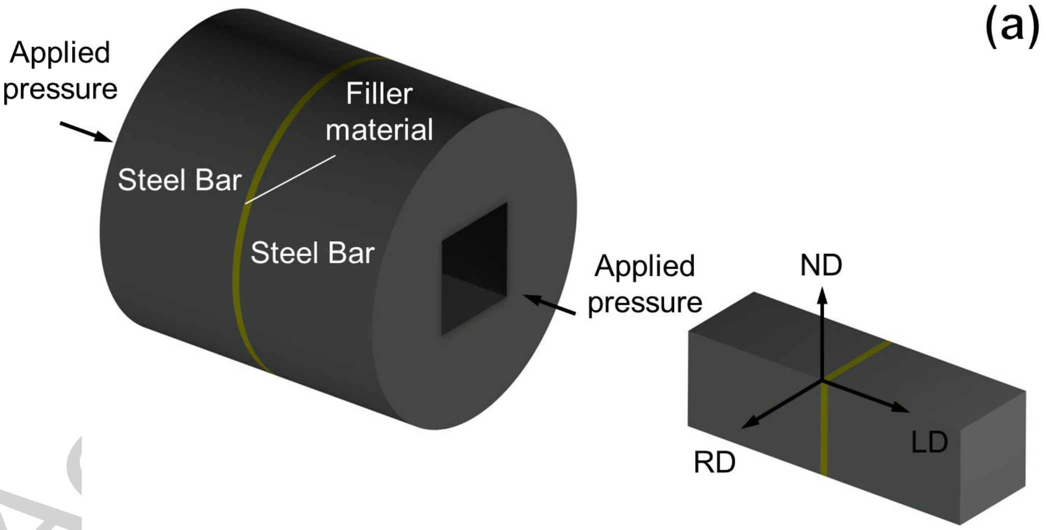

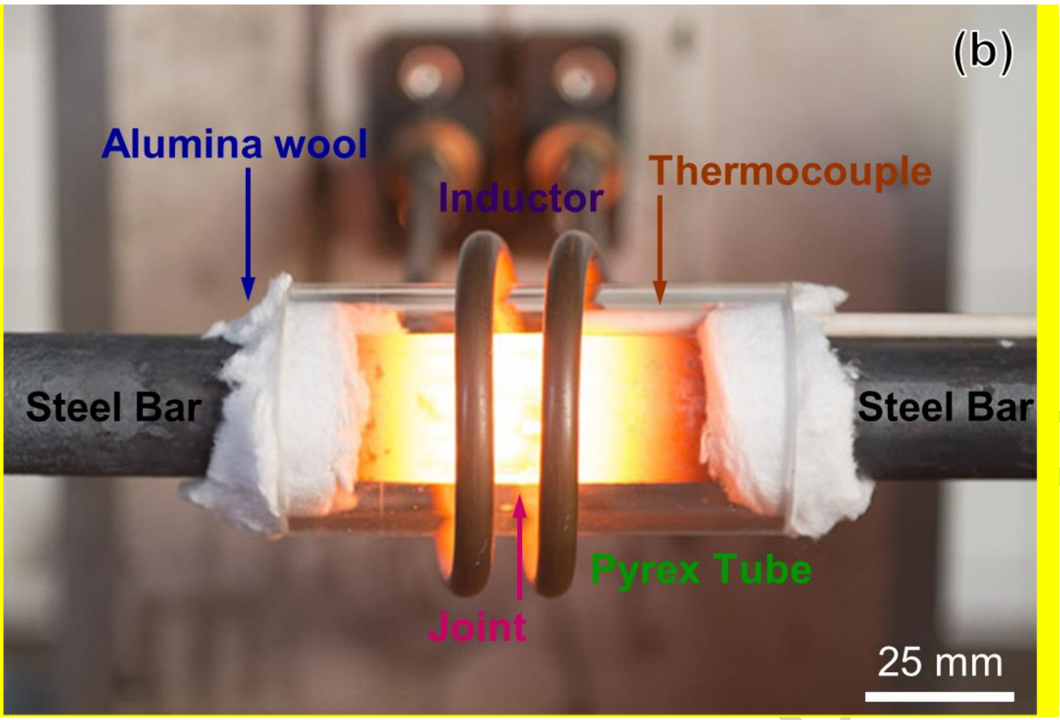

Fig. 1 (a) Scheme of the joint of the TLP-bonded bars. The position of the filler material with respect to the bars to be bonded and the direction of *p* are depicted. The square bar specimen cut by WEDM from the centre of the bonded sample is shown. The radial direction (RD), longitudinal direction (LD) and normal direction (ND) are also indicated; (b) Image during the TLPB process, in which it is highlighted the position of the joint, the inductor of the induction furnace, the thermocouple, the Pyrex tube to contain Ar atmosphere, and the alumina wool to seal between the Pyrex tube and the steel bars

2.2 Quantitative B concentration measurement

The B concentration profile across the joint was determined by means of NR on the ANTARES beamline at the Forschungs-Neutronenquelle Heinz Maier-Leibnitz (FRM II). The experimental arrangement was the same as that described by Schulz *et al* [22] and Di Luozzo *et al* [18]. A beam collimation ratio L/D = 500 was used, where L and D are the collimator length and its aperture diameter, respectively. The images obtained by a Gd_2O_2S scintillator were projected by a mirror and a Leica 100 mm f/2.8 macro lens onto an Andor Neo sCMOS camera (2560x2160 pixels), giving an effective pixel size of 19.8 μm/pixel. As a result, a spatial resolution of ≈ 50 μm was obtained.

At any point in the obtained NR image, the normalized transmittance τ was calculated as follows:

$$\tau = \frac{I}{I_0} = \frac{ID - DI}{OB - DI} \qquad (1)$$

where I_0 is the incident neutron intensity, I is the transmitted neutron intensity, and *ID*, *OB* and *DI* are the image data, open beam and dark image conditions, respectively. Stacks were recorded to obtain the final images in each condition: 345 images for both *ID* and *OB* conditions and 18 images for *DI* condition. The exposure time for each image was 90 s. Median filtering only along LD was used in the final τ image to improve the signal-to-noise relationship. For further details regarding NR, see reference [18].

2.2.1. Calculation procedure

In addition to equation (1), τ can also be calculated by means of the Beer-Lambert transmittance law:

$$\tau = \frac{I}{I_0} = e^{-\bar{\mu}\, w} \qquad (2)$$

where $\bar{\mu}$ is the mean linear attenuation coefficient for a given neutron energy spectrum and w is the thickness of the sample. Specifically, we are interested in the normalized transmittance per unit thickness τ'. From equation (2), we obtain:

$$-\ln \tau' = \bar{\mu}' \qquad (3)$$

where $\bar{\mu}'$ is the mean linear attenuation coefficient for a given neutron energy spectrum per unit thickness (w = 1 cm).

Except for the traces of borides [2] at the joint, the same microstructure is observed throughout the sample (see Section 3.1. Microstructural analysis). Therefore, the only difference between the joint and the base metal is its B concentration: the higher the B concentration is, the greater the neutron absorption and, consequently, the lower the transmittance. In addition, we assume that all the B content is soluble B and that the maximum B concentration is within the specified range of B-alloyed carbon steels - 30 ppm maximum (e.g., Class 8.8 [23]).

Considering the high absorption cross section of ^{10}B, with an abundance of 19.4% in natural B [24], and equation (3), at any given point of the sample, we have:

- at the base metal: $-\ln \tau'_{Base\ Metal} = \bar{\mu}'_{Base\ Metal}$ (4)
- at the joint [25]:

$$-\ln \tau'_{Joint} = \bar{\mu}'_{Joint} = \rho_{Joint} \left[\omega_{Base\ Metal} \frac{\bar{\mu}'_{Base\ Metal}}{\rho_{Base\ Metal}} + \omega_B \frac{\bar{\mu}'_B}{\rho_B} \right] \qquad (5)$$

---

[2] Borides are formed from the remaining liquid phase after t_h at T_P and solidifies during cooling.

where ω and ρ are the mass fraction and the density, respectively. However, we know that at the joint [18]:

$$\omega_B = 1\times10^{-5} / 2\times10^{-5} \qquad \text{and} \qquad \omega_{Base\ Metal} \cong 1 \qquad (6)$$

Therefore, considering (6), we can assume the following:

$$\rho_{Joint} \cong \rho_{Base\ Metal} \qquad (7)$$

Finally, equation (5) can be rewritten as:

$$\left(\ln \tau'_{Base\ Metal} - \ln \tau'_{Joint}\right) \frac{\rho_B}{\rho_{Base\ Metal}} \frac{1}{\bar{\mu}'_B} = \omega_B \qquad (8)$$

$\bar{\mu}'_B$ in low carbon B-alloyed steels was already measured for the ANTARES energy spectrum - 424.8 cm^{-1} [18]. Therefore, for a given τ profile across the joint, ω_B can be calculated from equation (8).

2.3. X-ray microdiffraction

Microfocused X-ray microdiffraction was performed at beamline ID27 of the European Synchrotron Radiation Facility (Grenoble, France) [26] in transmission geometry. A microfocused - 4.5 x 4.5 µm^2 - high resolution monochromatic beam was achieved by two bent Kirkpatrick-Baez mirrors.

A 20 µm thick sample from the joint and the neighbouring base metal enabled a proper transmission signal [3] and allowed direct microfocusing on borides with low detection

---

[3] A 1 mm thick sample was cut from a square bar specimen (as shown in Fig. 1 (a)), which was thinned down to 20 µm by grinding.

volume limits (~ below 500 μm^3) when combined with a microfocused beam and micropositioning of the sample.

X-ray diffraction patterns were recorded with a Perkin-Elmer flat 2D panel detector, and the sample was rocked ± 15°, with an acquisition time of 10 sec for each collected image with a step size of one degree. Lanthanum hexaboride (LaB_6) powder (NIST Standard Reference Materials 660c [27]) was used to calibrate the detector geometry and wavelength (0.37631(3) Å) using the Dioptas graphical interface [28] and pyFAI [29] calibration procedure. Subsequently, the Dioptas graphical interface and pyFAI integration procedure were used to integrate the 2D experimental data to obtain 1D intensity vs 2θ diffraction patterns.

Analysis of the diffraction data based on Rietveld analysis of the full profile was performed using the GSAS-II [30] suite package.

2.4. Mechanical properties characterization

2.4.1. Tension tests

Tension tests were conducted to provide information on the strength and ductility of the bonded samples under uniaxial tensile stresses according to ASTM E8M [31].

From the tension tests, the ultimate tensile strength (UTS), *e* and reduction area (q) were measured.

Standard round tension test specimens with a diameter of 12.5 mm and gauge length of 62.5 mm were machined from the bonded samples.

2.4.2. Bend tests

Bend tests on test specimens taken from the bonded samples were carried out according to ISO 5173:2023 [32] to determine their ductility on or near the surface.

The tests were carried out by placing the test specimens on two parallel rollers, with the joint at the midpoint between the rollers. The tests were completed when the specimen was ejected from the bottom of the fixture.

Regarding the shape and dimensions of the test specimens, bars 13 mm in diameter and 180 mm in length were machined from the bonded samples. The diameter of the former was 52 mm, the distance between the rollers was 78 mm, and the roller diameter was 30 mm. Therefore, the elongation *e* on or near the surface was 20%.

3. Results

3.1. Microstructural analysis

The microstructure at the base metal is composed of ferrite and pearlite (Fig. 2) in the same way as the joint (Fig. 3). Inclusions smaller and bigger than 5µm - from now on, small and large inclusions, respectively - can be seen. In fact, traces of inclusions are the only reference for the position of the bonding surfaces after the TLPB process (Fig. 3, dashed line). Therefore, a ferritic/pearlitic microstructure is observed throughout the joint. Small (Fig. 3, arrow mark) and large inclusions (Fig. 4) are found in the middle of the joint.

Away from the joint, the heat affected zone (HAZ) is observed. In this zone, the grain growth of the ferritic/pearlitic microstructure of the cold-finished base metal due to the thermal cycle of the TLPB process (Fig. 5) is evident.

Regarding grain size, a statistical analysis was carried out according to ASTM E112-13 (2021) [33]:

- Base metal (ferrite grains) - Mean Lineal Intercept Length (l) = 16.5 µm; Standard Deviation (s) = 3.0 µm; 95 % Confidence Interval (95% CI) = 2.2 µm; Percent relative accuracy (% RA) = 13.2; ASTM Grain Size Nº (G) = 8.5 ± 0.5.
- HAZ (ferrite grains) - l = 17.6 µm; s = 3.0 µm; 95% CI = 2.2 µm; % RA = 12.4; G = 8.5 ± 0.5.
- HAZ (pearlite grains) - l = 96.6 µm; s = 17.4 µm; 95% CI = 12.5 µm; % RA = 12.9; G = 3.5 ± 0.5.

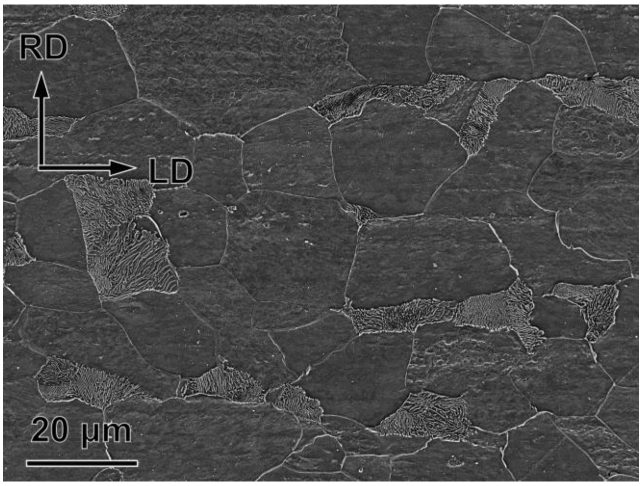

Fig. 2 Microstructure characterization of the base metal by SEM. The dark and light microconstituents correspond to ferrite and pearlite, respectively. In addition, the scale bar and RD and LD are indicated

Fig. 3 Microstructure characterization at the joint by SEM showing the ferritic/pearlitic microstructure (dark and light microconstituents correspond to ferrite and pearlite, respectively). A small inclusion and the estimated position of the middle of the joint are denoted with an arrow and a dashed line, respectively. In addition, the scale bar and RD and LD are indicated

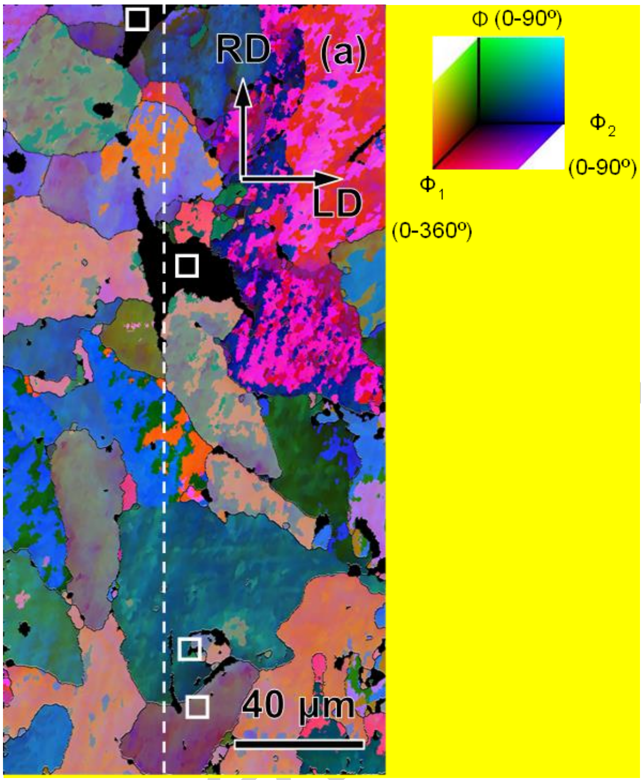

Fig. 4 Microstructure characterization by EBSD at the joint where large inclusions were found. Euler-coloured orientation image map of Fe-BCC, together with the coloured space used for the Euler angle description. Grain boundaries ($\theta > 5°$, where θ is the misorientation angle) are denoted with black lines. Large inclusions (square marks) together with the estimated position of the middle of the joint (dashed line) are denoted. In addition, the scale bar and RD and LD are also indicated

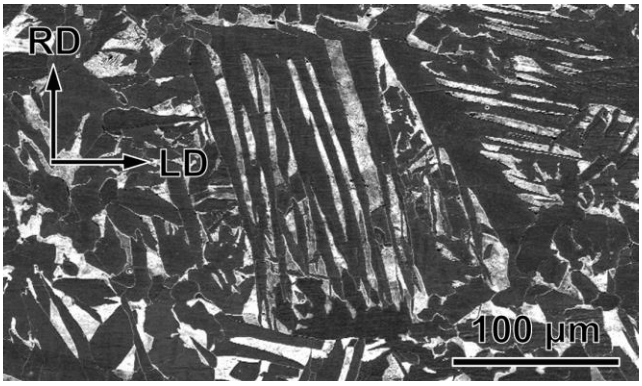

Fig. 5 Microstructure characterization of the HAZ by SEM showing the ferritic/pearlitic microstructure. The grain growth of the microstructure of the base metal is evident due to the thermal cycle of the TLPB process. In addition, the scale bar and RD and LD are indicated

3.2. Chemical concentration profiles across the joint

3.2.1. B measurements by neutron radiography

The neutron radiography image of the bonded sample is shown in Fig. 6. A darker line parallel to RD is visible, which indicates the peak neutron absorption in the middle of the joint (Fig. 6; white arrow mark).

Fig. 7 shows the τ profile perpendicular to the joint from Fig. 6. With the aim of increasing the statistics, the τ profile is 6.5 mm width (Fig. 6; yellow shaded area). The base metal baseline can be distinguished as $\tau = 0.4082$. In addition, a broad τ dip (base width of $\approx$ 5 mm) can be observed, with a sharp minimum dip in the middle of the joint (Fig. 7; arrow mark).

By means of equation (8), the B profile was calculated and is shown in Fig. 8. At the middle of the joint, a sharp peak with a maximum value of 15.9 ppm B is superimposed over a broad peak with a base width of ≈ 5 mm and a maximum value of 13.3 ppm B. The broad peak corresponds to the diffusion of B from the filler material to the base metal during the TLPB process, while the sharp peak corresponds to the presence of traces of borides at the middle of the joint.

The error estimation of the B concentration measurements, ΔB, was carried out by evaluating the transmittance noise at the base metal in Fig. 6. The transmittance error bound $\Delta\tau = 7 \times 10^{-4}$ was measured, and through equation (8), we obtained ΔB = 1 ppm B.

3.2.2. EPMA measurements

The Mn and Si gradients across the joint are shown in Fig. 9. A small impoverishment of these elements can be seen at the joint. This is due to the alloying elements of the filler material. To carry out the TLPB, the filler material - a eutectic Fe-B alloy - was positioned between the bars to be bonded. However, B from the filler material rapidly diffused into the base metal during the TLPB process, with a final concentration of a few tenths of ppm B or less. As a result, diluted Mn and Si concentrations were found at the joint with respect to the base metal.

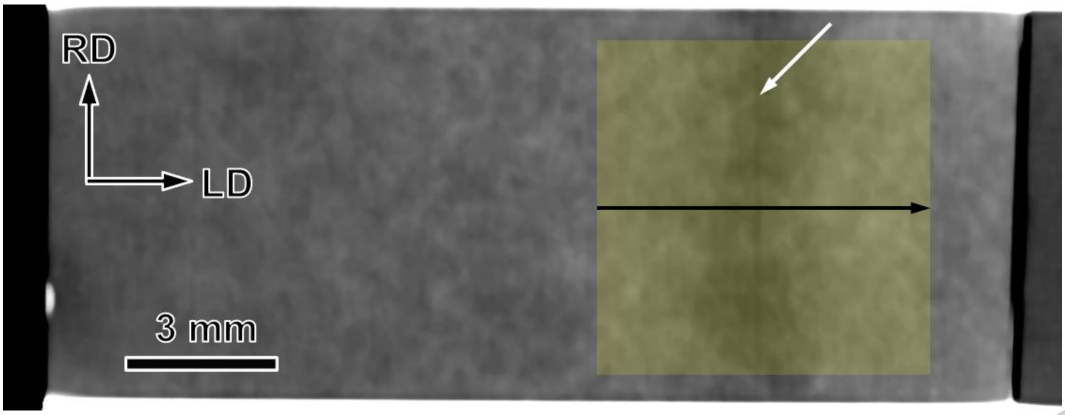

Fig. 6 Neutron radiography image of the sample. The darker line parallel to RD indicates the peak neutron absorption in the middle of the joint (white arrow). The yellow shaded area indicates the analysed area, and the black arrow indicates the direction of the τ profile shown in Fig. 7. At both ends of the sample, clamping devices can be observed. In addition, the scale bar and RD and LD are indicated

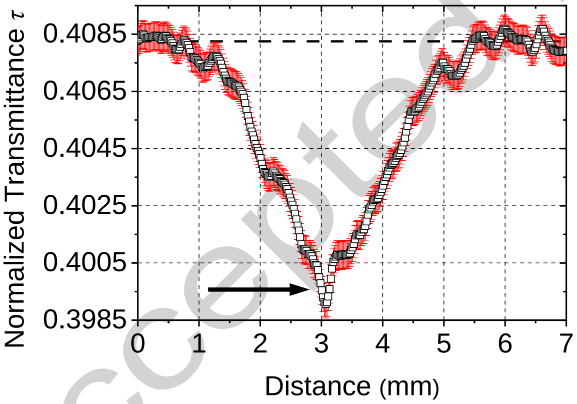

Fig. 7 Normalized transmittance τ profile (black rectangles) across the joint and the base metal next to it. The base metal transmittance of 0.4082 is indicated (dashed line). A wide τ dip, accompanied by a sharp minimum dip in the middle of the joint, can be seen (arrow mark). In addition, the error bars (in red) based on the transmittance error bound - $\Delta\tau$ - 5 x 10^{-4} - are shown

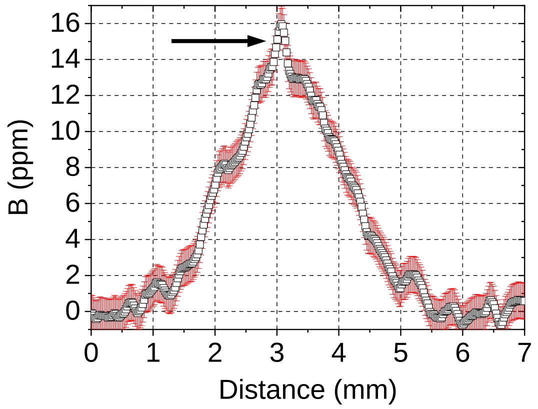

Fig. 8 B concentration profile obtained by neutron radiography (black rectangles) across the joint and the base metal next to it. A sharp peak concentration (arrow mark) is superimposed over the B gradient across the joint. In addition, the error bars (in red) based on the estimation of the B concentration measurement error ΔB - 1 ppm B - are shown

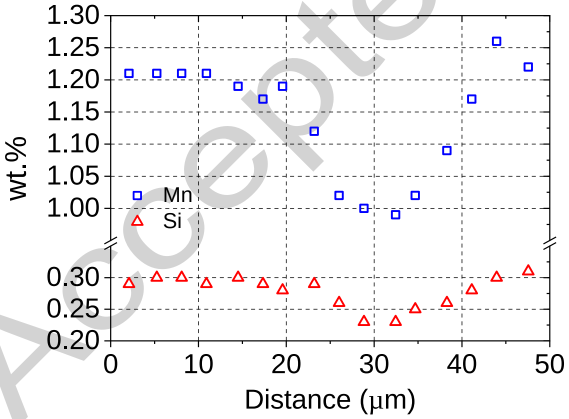

Fig. 9 Mn and Si concentration profiles obtained by EPMA (blue rectangles and red triangles, respectively) across the joint

3.2.3. EDS measurements at inclusions

EDS qualitative map and quantitative point and zone measurements at small and large inclusions were carried out at the middle of the joint.

In Fig. 10 an EDS qualitative maps of Fe, O, Mn and Si are shown, corresponding to a small inclusion. At the cross mark, a point EDS measurement was done (spectrum results are shown in Table 2). In addition, C on the surface of the sample from hydrocarbon-based contaminants was also detected in all EDS measurements.

Another small inclusion - shown in Fig. 11 - was analysed with an EDS quantitative point measurement. Fe, Al, Mn and Si were detected (spectrum results are shown in Table 2).

On the other hand, an example of a large inclusion is shown in Fig. 12, where an EDS qualitative maps of Fe, O, Mn and Si and an EDS quantitative zone measurement was carried out (Fig. 12 rectangle mark). Fe, O, Al, Si and Mn were detected (spectrum results are shown in Table 2).

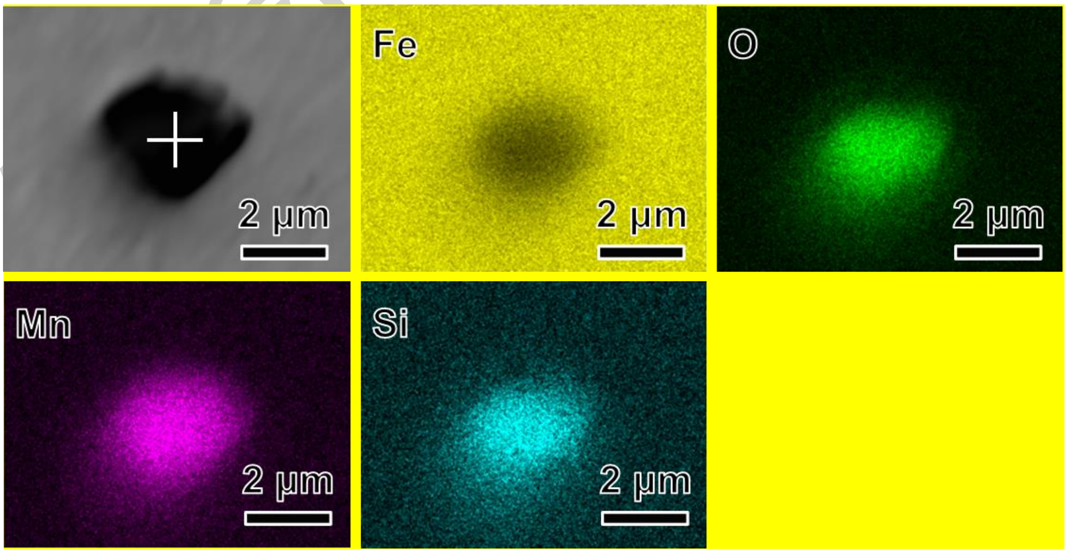

Fig. 10 EDS qualitative maps of Fe, O, Mn and Si of a small inclusion at the middle of the joint. A cross mark indicates where the EDS quantitative point measurement was carried out. In addition, scale bars are shown

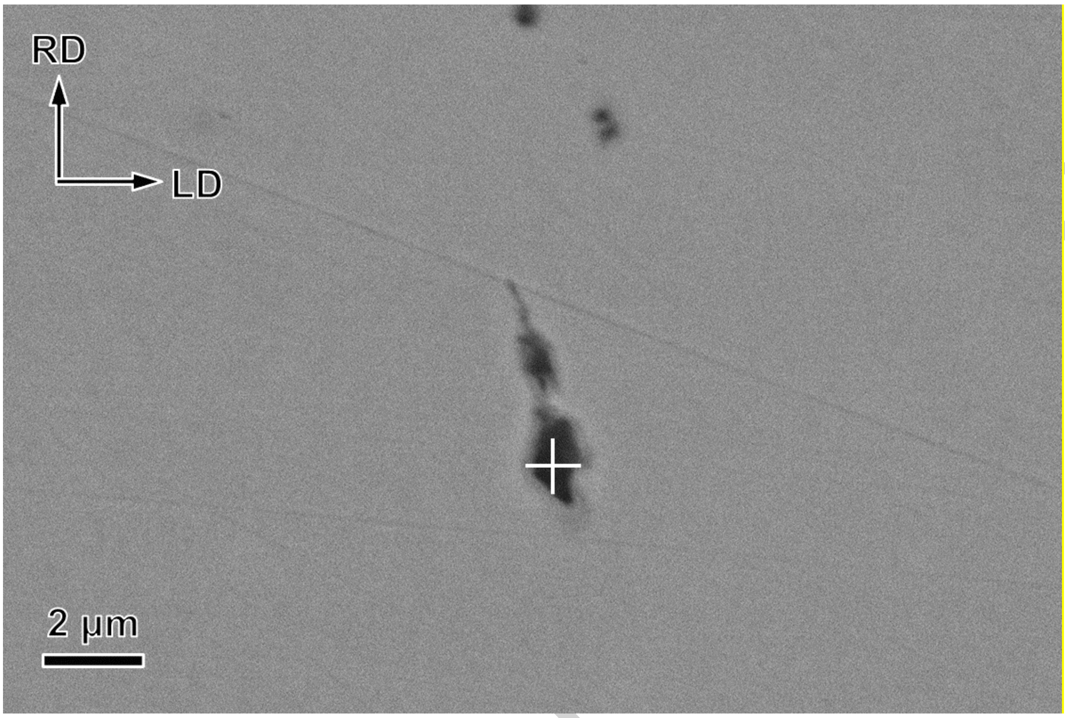

Fig. 11 EDS quantitative point measurement at another small inclusion at the middle of the joint. A cross mark indicates where EDS was carried out. In addition, a scale bar is shown

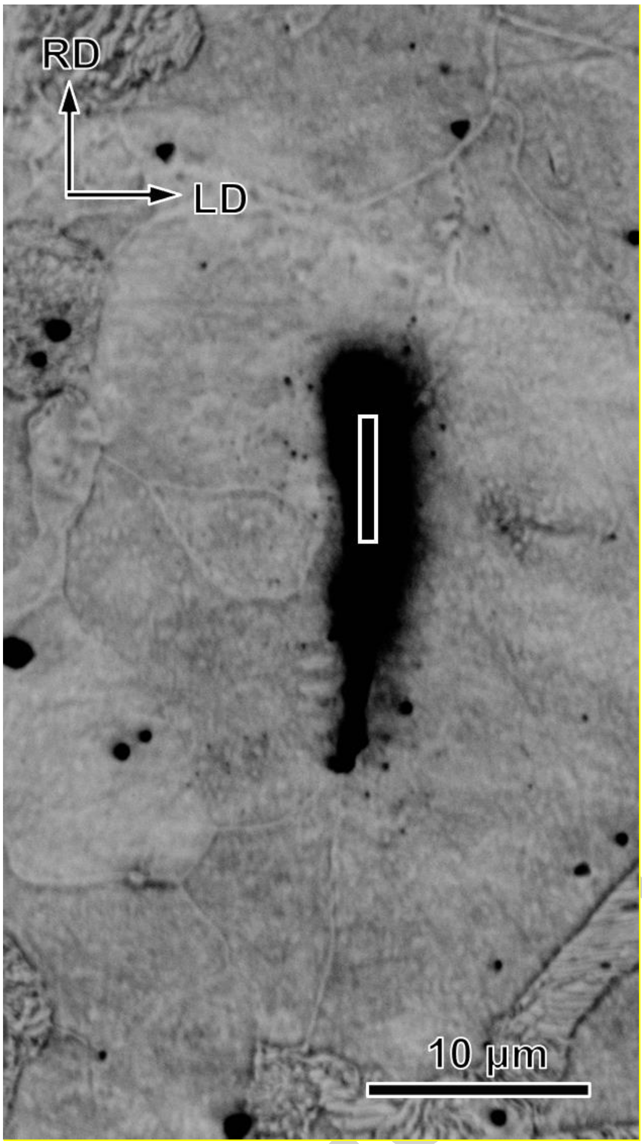

Fig. 12 Large inclusion at the middle of the joint in which EDS qualitative maps and quantitative zone measurements were carried out. In addition, a scale bar is shown

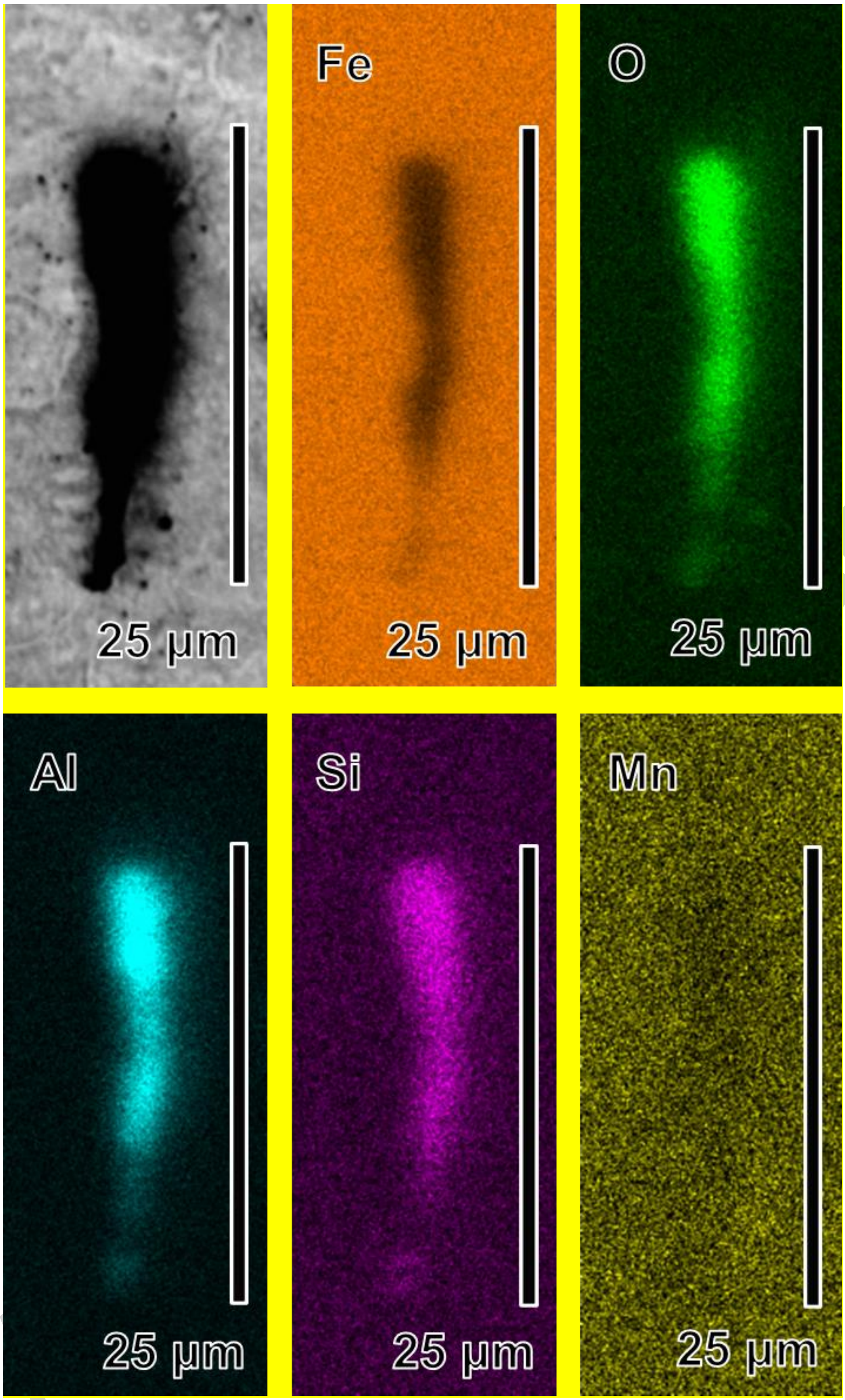

Fig. 13 EDS qualitative maps of Fe, O, Al Si and Mn of the large inclusion in Fig. 12. In addition, scale bars are shown

Table 2

EDS quantitative measurements results, in wt.%. The standard deviation is indicated in brackets.

Figure	C	Fe	Mn	Si	Al	O
10	16.8 (0.3)	42.2 (0.2)	18.3 (0.2)	3.4 (0.1)	0.5 (0.0)	18.9 (0.2)
11	16.7 (0.3)	80.9 (0.3)	0.96 (0.08)	0.20 (0.04)	-	1.28 (0.11)
12	9.1 (0.2)	77.3 (0.3)	0.6 (0.1)	1.2 (0.0)	5.1 (0.1)	6.7 8 (0.1)

3.3. Large inclusion structure determination

The results of Rietveld refinement using GSAS-II performed on one of the large inclusions are shown in Fig. 14. Ferrite and $Fe_{23}B_6$ boride cubic phases and an Fe_3C structure type orthorhombic phase (present in the form of minor traces) were used in the refinement. The final agreement parameters were an unweighted profile R factor (R_p) = 5.789% and a weighted profile R factor (R_{wp}) = 7.819%. The cell parameters are 2.86406(5) Å for ferrite, 10.6801(2) Å for $Fe_{23}B_6$ and a = 5.055(2) Å, b = 6.726(2) Å and c = 4.537(2) Å for the Fe_3C structure type phase.

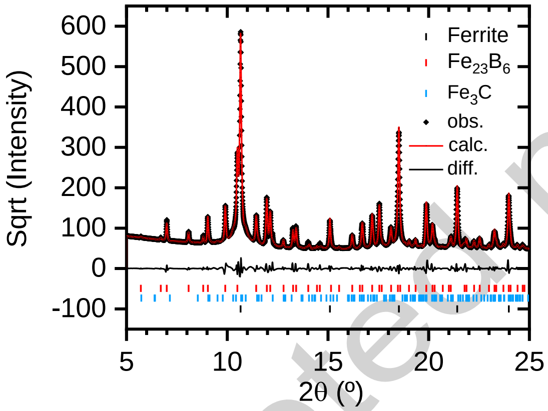

Fig. 14 Results of Rietveld refinement using GSAS-II for the ferrite, $Fe_{23}B_6$ and Fe_3C structure type phases

3.4. Mechanical properties

3.4.1. Tension tests

The results of the tension tests are shown in Fig. 15 and Table 3. Three specimens were tested from the base metal and the bonded samples. The average value and error of UTS and *e* are indicated.

From Fig. 15 and Table 3, we observe that the bonded samples attain an UTS of 434 MPa, an *e* of 32.3% and a *q* of 51.2% - 78.6%, 165.6% and 75.4%, respectively, of the base metal.

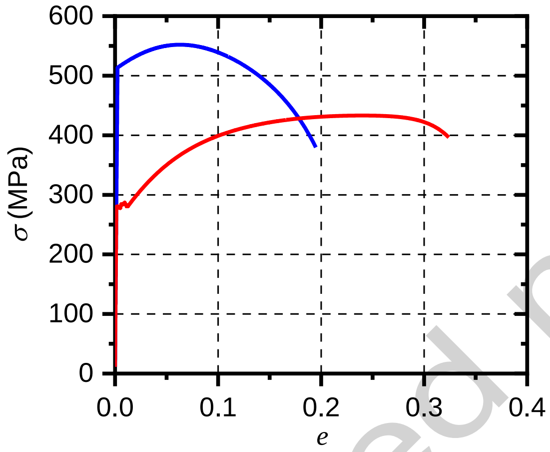

Fig. 15 Stress-strain curves of one of the specimens from the base metal (blue line) and the bonded sample (red line)

Table 3

Average mechanical properties determined in the tension test. The errors are indicated in brackets.

	UTS (MPA)	*e* (%)	*q* (%)	Fracture position
Base Metal	552 (11)	19.5 (0.4)	67.9 (5.5)	Not applicable
Bonded Sample	434 (9)	32.3 (0.4)	51.2 (2.3)	At the joint

3.4.2. Bend tests

The results of the bend tests are shown in Table 4. Three specimens from the bonded samples were tested. The average value and the error of the peak charge are indicated. Since the measured *e* of the base metal was 19.5 ± 0.4, the bend test was carried out at the standard value of *e* = 20%, with a bend angle of 180º. As a result, no cracks were observed.

Table 4

Bend test results for the base metal and bonded samples. The errors are indicated in brackets.

Specimen (°)	Peak charge (N)	Fracture appearance
Base metal	19581 (392)	Absence of imperfections
Bonded sample	13930 (290)	Absence of imperfections

4. Discussion

4.1 Types of inclusions at the middle of the joint

Llovet *et al* [34] showed the difficulty of measuring quantitatively B by EPMA. Portebois *et al* [35] only measured B by EPMA and the rest of the elements by EDS in Nb alloys. These difficulties are mainly due to:

- Overlapping X-ray lines
- Chemical bonding effects on peak position between standards and samples to be measured
- Large potential error due to large absorption of the elements of the matrix

In our case, with a steel matrix, B was not detected by EDS. Therefore, it was detected indirectly: inclusions with a noticeable Fe content and small amounts of other elements were assumed to be composite inclusions with borides.

From Table 2, we can determine:

- In Fig. 10 the small composite inclusion consists in a small boride with MnO and traces of SiO_2-Al_2O_3.
- In Fig. 11 the small composite inclusion consists in a small boride with traces of MnO.
- In Fig. 12 the large composite inclusion consists in a large boride with Al_2O_3 and traces of MnO-$Si0_2$.

These composite inclusions containing borides took place due to:

- Borides at the middle of the joint are the result of the liquid phase that solidified during the cooling stage.

- During solidification, any insoluble inclusions within the liquid phase are dragged by the solid-liquid interfaces towards the middle of the joint [36].

Consequently, the final solidification product are composite inclusions composed mostly of borides - in particular the $Fe_{23}B_6$ cubic phase , and of varying contents of Al_2O_3, MnO and $Si0_2$.- which are common inclusions in steel.

4.2. Formation of $Fe_{23}B_6$ at the joint

From microfocused X-ray microdiffraction, it was determined that borides were composed of $Fe_{23}B_6$ ($Fe_{95.19}B_{4.81}$ wt.% ($Fe_{79.31}B_{20.69}$ at.%)), a metastable compound of the Fe-B system [37].

Regarding borides in B-alloyed steels, the phase that has been detected the most is $Fe_{23}(B,C)_6$ - and not the equilibrium Fe_2B - at PAGBs [38][39][40][41]. In particular, $Fe_{23}(B,C)_6$ precipitates at the most favourable nucleation sites, e.g., at grain corners and grain edges [42]. However, the precipitation of Fe_2B took place at the expense of the dissolution of $Fe_{23}(B,C)_6$ at PAGBs after 600 s of holding time at 820 °C [43]. Fujishiro *et al* [44] obtained similar results with increasing holding times at 650 °C. Thus, with the proper post-weld heat treatment, the transformation of $Fe_{23}(B,C)_6$ into Fe_2B can be carried out.

Therefore, the stabilization of metastable $Fe_{23}B_6$ at room temperature in steels in the presence of B depends strongly on the thermal history of the steel sample - in our particular case, the thermal cycle of the TLPB, which is applied to the base metal.

4.3. Analysis of the tension and bend testing of the base metal and the bonded sample

Since TLPB testing standards of mechanical properties are not yet available, the American Petroleum Institute (API) Standard 1104 *Welding of Pipelines and Related Facilities* 22nd edition (2021) was used [45], in which the basic testing of arc welded joints is carried out by the tension and the bend tests.

Regarding the tension test, the Standard 1104 indicates that:

- If the specimen breaks outside the weld (i.e., in the base metal) at a tensile strength not less than 95 % of that of the specified minimum tensile strength (SMTS) of the base metal, the weld shall be accepted as meeting the requirements.
- If the specimen breaks in the weld and the observed strength is greater than or equal to the SMTS of the base metal, the weld shall be accepted as meeting the requirements.

Regarding the bend test, the Standard 1104 indicates that:

- The bend test shall be considered acceptable if no crack or other imperfection exceeding 3 mm or one-half the specified wall thickness, whichever is smaller.

As it was stated in Section 2.4, tension and bend tests were carried out according to ASTM E8M and ISO 5173, respecively.

Since TLPB has a thermal cycle that strongly promotes grain growth, it was assumed that the cold-drawn carbon steel bars lost their strain hardening at the joint, and that reference mechanical properties can be those of the steel bars in the hot rolled condition.

From SAE J1397_202403 *Estimated Mechanical Properties and Machinability of Steel Bars* [46],for a steel grade 1008 in the hot rolled condition we obtain :

- UTS: 303 MPa
- *e* (Estimated Minimum Values): 30 %
- *q*: 55 %

Therefore, and from the abovementioned criteria, the UTS, *e* and *q* of the bonded sample attained 143.2%, 107.6% and 93.1% of the reference material.

On the other hand, specimens from both the base metal and the bonded sample were subjected to bend test with the absence of imperfections.

Therefore, basic testing requirements of API Standard 1104 were attained. Anyway, *q* is below the reference value, which is discussed in Subsection 4.4. Decrease in the reduction area of the bonded specimens.

4.4. Decrease in the reduction area of the bonded specimens

The tension and bending tests revealed the strength and ductility of the bonded specimens (Fig. 15, Table 3 and Table 4). From these tests, the following conclusions can be drawn:

- The decrease in UTS of the bonded samples compared with that of the base metal is due to the recovery, recrystallization and grain growth that occurred during the TLPB thermal cycle.

- An increase in *e* of the bonded samples compared with that of the base metal occurred. This was the result of the base metal recovery and recrystallization processes prior to grain growth.

However, *q* of the bonded samples decreases compared with that of the base metal, which cannot be explained by these tests.

Therefore, the fracture surfaces of specimens from the tension test were observed by SEM:

- The base metal shows the classic cup-and-cone surface. Both the shear lip and the central fibrous zone correspond to ductile fractures (Fig. 16 (a) and (b), respectively).
- Apart from the small dimples and particles, as in the base metal, the bonded sample also shows larger dimples and particles than those observed in the base metal (Fig. 17). Considering that the only difference between the base metal and the bonded samples is the TLPB process, these larger particles must be composite inclusions composed mostly of borides. These composite inclusions, which are located only at the middle of the joint, have adverse effects on ductility and consequently on *q*.

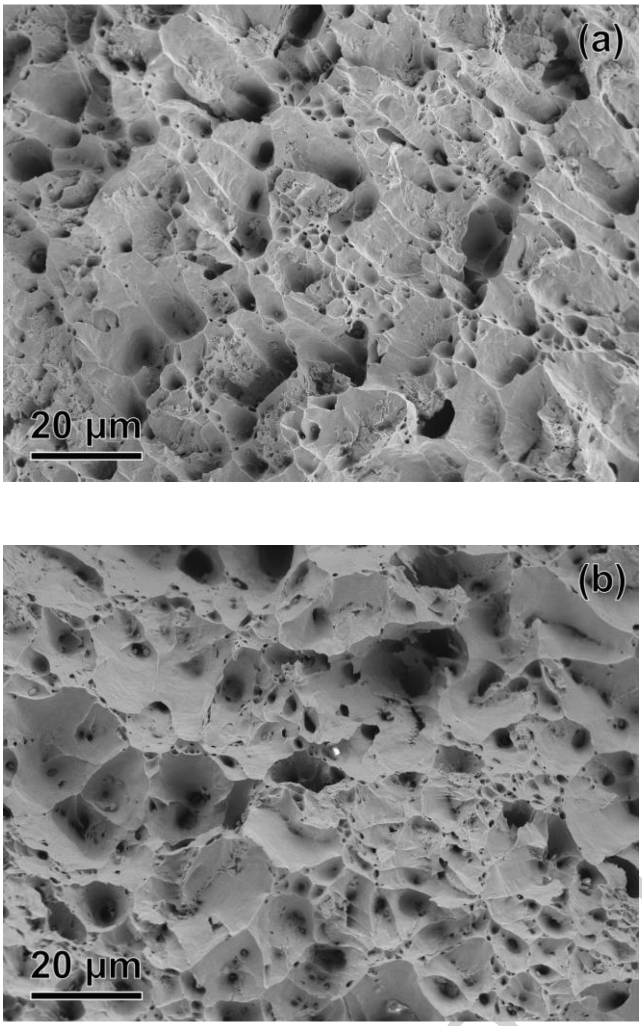

Fig. 16 Fracture surfaces of the base metal. Both in the shear lip (a) and in the fibrous central zone (b), dimples and particles corresponding to ductile fracture can be clearly identified. In addition, the scale bar is indicated

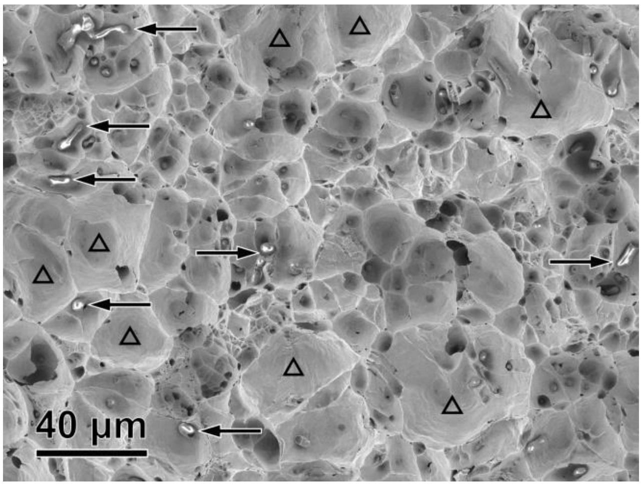

Fig. 17 Fracture surfaces of the bonded samples. Larger dimples with and without large inclusions (arrow marks and triangle marks, respectively) can be clearly identified. In addition, the scale bar is indicated

To reassure the latter stamen, composite inclusions at the fracture surface were characterised by EDS and analysed in a similar manner as in Subsection 4.1.

In Fig. 18 large inclusions are shown and Fig. 19 shows the qualitative map for Fe, Mn and Si. Table 5 shows the quantitative EDS measurements at the cross marks of Fig. 18. As a result, we obtain:

- At point 1 mostly Fe is detected, with traces of other elements.
- At point 2 mostly MnO is detected, with $Si0_2$, MnO and Al_2O_3, and traces of MnS and CaO. These are common inclusions in steel.

Therefore, from point 1 measurement, we can conclude that the large inclusion is a boride.

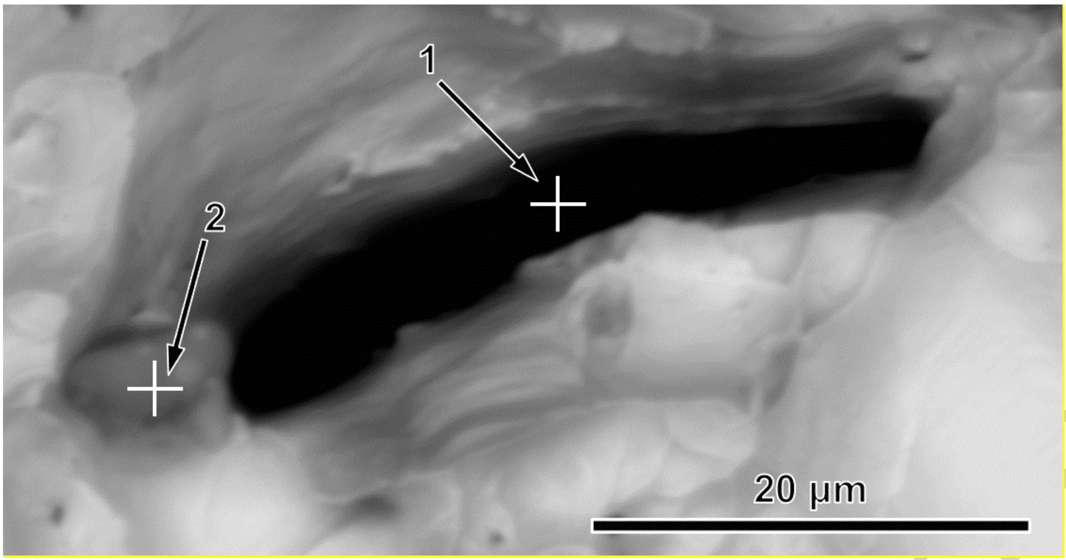

Fig. 18 Large inclusion at the fracture surface which EDS qualitative maps and quantitative point measurements were carried out. In addition, a scale bar is shown

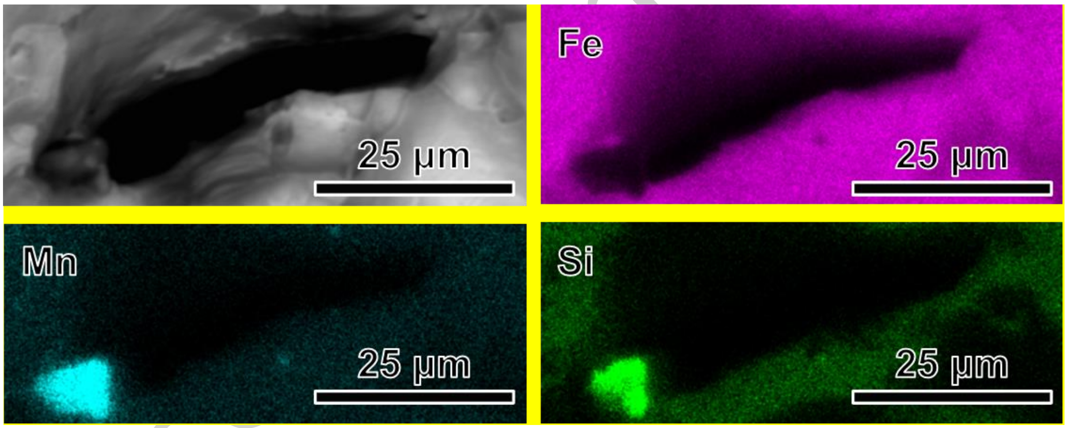

Fig. 19 EDS qualitative maps of Fe, Mn and Si of the large inclusion in Fig. 18. In addition, scale bars are shown

Table 5

EDS quantitative measurements results of Fig. 18, in wt.%. The standard deviation is indicated in brackets.

Point	C	Fe	Mn	Si
1	1.4 (0.1)	98.3 (0.1)	-	0.1 (0.0)
2	6.9 (0.3)	18.3 (0.2)	29.2 (0.2)	6.5 (0.1)
Point	Al	O	S	Ca
1	-	0.2 (0.0)	-	-
2	4.4 (0.1)	32.3 (0.2)	1.5 (0.0)	0.8 (0.0)

In Fig. 20 small inclusions are shown. It shows quantitative EDS points measurements at threes inclusions at their dimples and in Table 6 the corresponding measurements, from which we obtain:

we obtain:

- At point 1 Fe with Al_2O_3 and $Si0_2$ is detected, with traces of MnS.
- At point 2 mostly Fe is detected, with MnO Al_2O_3 and $Si0_2$,and traces of MnS.
- At point 3 mostly Fe is detected, with traces of other elements.

Therefore, at all points borides are detected - in particular at point 3. In addition, all oxides and sulphides are common inclusions in steel.

Consequently, we can conclude that both small and large inclusions are borides or composite inclusions composed of borides with varying concentrations.

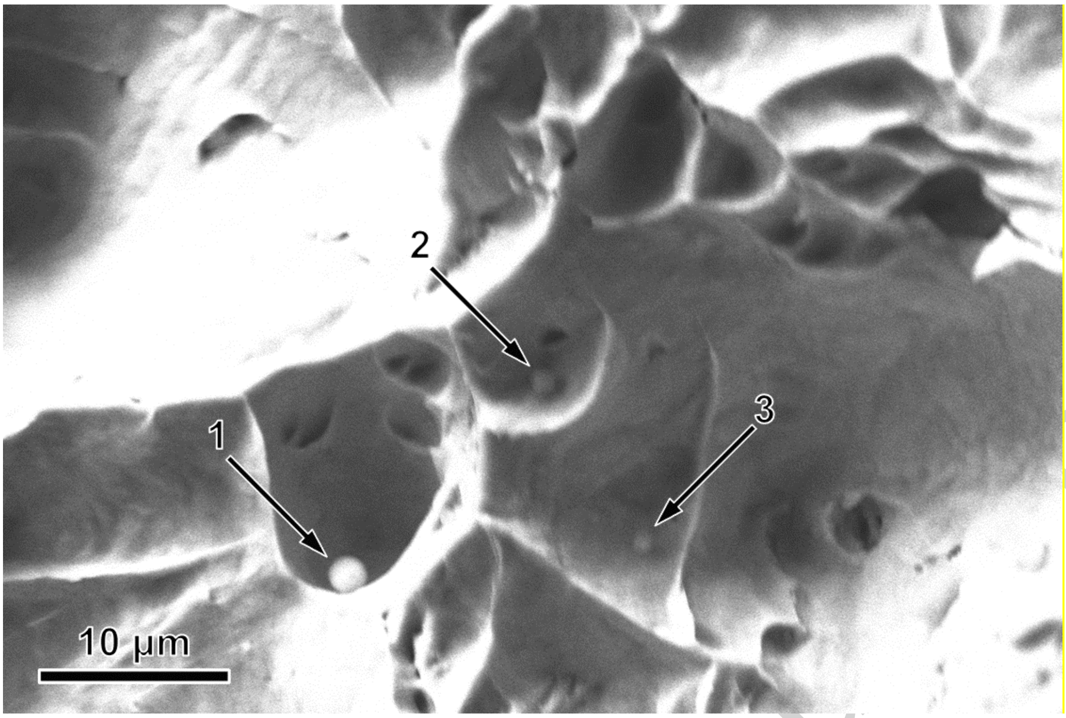

Fig. 20 EDS quantitative point measurement at small inclusions at fracture surface. Arrow marks indicate which inclusions were measured. In addition, a scale bar is shown

Table 6

EDS quantitative measurements results of Fig. 20, in wt.%. The standard deviation is indicated in brackets.

Point	C	Fe	Mn	Si
1	9.10 (0.2)	41.37 (0.33)	15.82 (0.14)	4.99 (0.05)
2	5.79 (0.16)	81.69 (0.50)	3.71 (0.05)	1.56 (0.03)
3	2.33 (0.11)	95.68 (0.49)	0.95 (0.05)	0.17 (0.02)
Point	Al	O	S	Ca
1	6.50 (0.06)	21.58 (0.19)	0.63 (0.02)	-
2	1.65 (0.03)	5.45 (0.07)	0.15 (0.02)	-
3	0.11 (0.02)	0.66 (0.03)	0.10 (0.02)	-

5. Conclusions

Bonded samples of cold-finished carbon steel bars were obtained by TLPB using amorphous metallic foils composed of eutectic Fe-B as filler material. Regarding their microstructure and mechanical properties, we can highlight the following:

- The joint exhibits the same ferritic/pearlitic microstructure as the base metal, avoiding the microstructure discontinuity typically found in brazed and TLP-bonded steel samples.
- The quantitative B concentration profile was measured throughout the joint by means of NR.
- The measured broad peak of B, with a base width of ≈ 5 mm and a maximum value of 13.3 ppm B, allows the suppression of boride precipitation at most of the joint.
- Traces of borides, which were the result of the liquid phase that solidified during cooling, were found at the joint. Their position agrees with the measured sharp peak of B, with a maximum value of 15.9 ppm B.
- Borides were identified as $Fe_{23}B_6$ by means of microfocused X-ray microdiffraction.
- Regarding mechanical properties, the bonded samples were subjected to a bend test, with a bending angle of 180°, and no cracks were observed. In tension tests, the bonded samples attained an ultimate tension strength of 434 MPa, an elongation of 32.3% and a reduction area of 51.2% - 78.6%, 165.6% and 75.4%, respectively, of the base metal. The fracture of the bonded samples occurred at the joint.

- It was determined that the decrease in UTS of the bonded samples compared with that of the base metal was due to recovery, recrystallization and grain growth during the TLPB process.
- From fracture surface observation, it was found that the decrease in the reduction area in the bonded samples was caused by the presence of traces of borides at the joint.

Acknowledgements

This work was supported by the Universidad de Buenos Aires [Grant No. 20020170200266BA].

This work is based upon experiments performed at the ANTARES instrument operated by FRM II at Heinz Maier-Leibnitz Zentrum (MLZ), Garching, Germany.

We acknowledge the European Synchrotron Radiation Facility (ESRF) for provision of synchrotron radiation facilities and we would like to thank M. Mezouar for fruitful discussions and inhouse beamtime on beamline ID27.

The invaluable support of Peter Svec Sr. - Institute of Physics, Slovak Academy of Sciences, Bratislava, Slovakia - who kindly provided the Fe-B glassy ribbon is also acknowledged.

The authors also wish to thank Dr. Gustavo Castellano (FaMAF, UNC - CONICET) and Mr. Javier Faig (INTECIN, CONICET).

CRediT authorship contributions

Nicolás Di Luozzo contributed to conceptualization, formal analysis, investigation, resources, writing - original draft, writing - review & editing, visualization, supervision, project administration and funding acquisition.

Michael Schulz contributed to software, validation, investigation, resources, data curation and writing - review & editing.

Michel Boudard contributed to software, formal analysis, investigation, writing - original draft and writing - review & editing.

Silvina Limandri contributed to software, formal analysis, investigation, resources, data curation and writing - review & editing.

Gastón Garbarino contributed to formal analysis, investigation, resources, data curation and writing - review & editing.

Marcelo Fontana contributed to resources and writing - review & editing.

Declarations

Competing interests

The authors declare that they have no known competing financial interests or personal relationships that could have appeared to influence the work reported in this paper.

Data availability

The data will be made available upon request.

References

1. American Welding Society (2007) Brazing Handbook, 5th ed. American Welding Society, Miami
2. International Organization for Standardization (2016) ISO 17672:2016 Brazing Filler metals. https://www.iso.org/standard/63627.html. Accessed 4 Mar 2024
3. Xie C, Deng K, Teng J, et al (2023) Microstructural evolution and mechanical properties of Ni-based superalloy joints brazed using a ternary Ni-W-B amorphous brazing filler metal. J Alloys Compd 960:170663. https://doi.org/https://doi.org/10.1016/j.jallcom.2023.170663
4. Li S, Peng Y, Du Y, et al (2022) Microstructural characteristics and mechanical properties of IC10 superalloy and (CoCrNi)94Al3Ti3 MEA joint brazed using NiCrSiB filler. Mater Charact 189:111964. https://doi.org/10.1016/j.matchar.2022.111964
5. Li G, Zhang P, Shi H, Yu Z (2018) Microstructure and properties of Cr18-Ni8 steel joints brazed with BNi7+3%Cu composite solder. Vacuum 148:303–311. https://doi.org/10.1016/j.vacuum.2017.12.001
6. Duvall DS, Owczarski WA, Paulonis DF (1974) TLP Bonding: a New Method for Joining Heat Resistant Alloys. Weld J 53:203–214
7. Tuah-Poku I, Dollar M, Massalski TB (1988) A study of the transient liquid phase bonding process applied to a Ag/Cu/Ag sandwich joint. Metallurgical Transactions A 19:675–686. https://doi.org/10.1007/BF02649282
8. Di Luozzo N, Boudard M, Fontana M (2019) Transient liquid phase bonding of carbon steel components using Ni-based foils – A comprehensive joint characterization. Materials Science and Engineering: A 751:51–61. https://doi.org/10.1016/j.msea.2019.02.050
9. Wang X, Li X, Wang C (2013) Effect of two-step heating process on joint microstructure and properties during transient liquid phase bonding of dissimilar materials. Materials Science and Engineering: A 560:711–716. https://doi.org/10.1016/j.msea.2012.10.018
10. Totten GE (2006) Steel Heat Treatment: Metallurgy and Technologies, 2nd ed. Taylor & Francis Group, Boca Raton
11. Di Luozzo N, Doisneau B, Boudard M, et al (2014) Microstructural and mechanical characterizations of steel tubes joined by transient liquid phase bonding using an amorphous Fe–B–Si interlayer. J Alloys Compd 615:S18–S22. https://doi.org/10.1016/j.jallcom.2013.11.161
12. Li W, Li X, Liu Y, et al (2020) Homogenization stage during TLP bonding of RAFM steel with a Fe–Si–B interlayer: Microstructure evolution and mechanical properties. Materials Science and Engineering: A 780:139205. https://doi.org/10.1016/j.msea.2020.139205

13. Bhadeshia H, Honeycombe R (2017) Solutes that Substitute for Iron. In: Bhadeshia H, Honeycombe R (eds) Steels: Microstructure and Properties, 4th ed. Butterworth-Heinemann, Kidlington, pp 101–134

14. Naz GJ, Dong D, Geng Y, et al (2017) Composition formulas of Fe-based transition metals-metalloid bulk metallic glasses derived from dual-cluster model of binary eutectics. Sci Rep 7:9150. https://doi.org/10.1038/s41598-017-09100-9

15. Burrier H (2013) Steel Heat Treating Fundamentals and Processes. In: Dossett JL, Totten GE (eds) ASM Handbook Volume 4A Steel Heat Treating. Fundamentals and Processes. ASM International, Materials Park, pp 26–59

16. International Organization for Standardization (2016) ISO 683-2:2016 Heat-treatable steels, alloy steels and free-cutting steels. Part 2: Alloy steels for quenching and tempering. https://www.iso.org/standard/70643.html. Accessed 4 Mar 2024

17. Di Luozzo N, Fontana M, Arcondo B (2008) Transient liquid phase bonding of steel using an Fe–B interlayer: microstructural analysis. J Mater Sci 43:4938–4944. https://doi.org/10.1007/s10853-008-2720-0

18. Di Luozzo N, Schulz M, Fontana M (2020) Imaging of boron distribution in steel with neutron radiography and tomography. J Mater Sci 55:7927–7937. https://doi.org/10.1007/s10853-020-04556-z

19. ASTM A108 - 18 (2018) Standard Specification for Steel Bar, Carbon and Alloy, Cold-Finished. https://doi.org/10.1520/A0108-18

20. Di Luozzo N, Boudard M, Fontana M, Arcondo B (2016) Effective diffusion coefficient for Cu in steel joined by transient liquid phase bonding. Mater Des 92:760–766. https://doi.org/10.1016/j.matdes.2015.12.101

21. Hielscher R, Silbermann CB, Schmidl E, Ihlemann J (2019) Denoising of crystal orientation maps. J Appl Crystallogr 52:984–996. https://doi.org/10.1107/S1600576719009075

22. Calzada E, Gruenauer F, Mühlbauer M, et al (2009) New design for the ANTARES-II facility for neutron imaging at FRM II. Nucl Instrum Methods Phys Res A 605:50–53. https://doi.org/10.1016/j.nima.2009.01.192

23. International Organization for Standardization (2013) ISO 898-1:2013 Mechanical properties of fasteners made of carbon steel and alloy steel. Part 1: Bolts, screws and studs with specified property classes. Coarse thread and fine pitch thread. https://www.iso.org/standard/60610.html. Accessed 4 Mar 2024

24. Albert-Jose Dianoux, Gerry Lander (2003) Institut Laue-Langevin Neutron Data Booklet, 2nd ed. Old City Publishing, Grenoble

25. Jackson DF, Hawkes DJ (1981) X-ray attenuation coefficients of elements and mixtures. Phys Rep 70:169–233. https://doi.org/10.1016/0370-1573(81)90014-4

26. Mezouar M, Crichton WA, Bauchau S, et al (2005) Development of a new state-of-the-art beamline optimized for monochromatic single-crystal and powder X-ray diffraction under extreme conditions at the ESRF. J Synchrotron Radiat 12:659–664. https://doi.org/10.1107/S0909049505023216

27. Black DR, Windover D, Henins A, et al (2011) Certification of Standard Reference Material 660B. Powder Diffr 26:155–158. https://doi.org/10.1154/1.3591064

28. Prescher C, Prakapenka VB (2015) DIOPTAS: a program for reduction of two-dimensional X-ray diffraction data and data exploration. High Press Res 35:223–230. https://doi.org/10.1080/08957959.2015.1059835

29. Kieffer J, Valls V, Blanc N, Hennig C (2020) New tools for calibrating diffraction setups. J Synchrotron Radiat 27:558–566. https://doi.org/10.1107/S1600577520000776

30. Toby BH, Von Dreele RB (2013) GSAS-II : the genesis of a modern open-source all purpose crystallography software package. J Appl Crystallogr 46:544–549. https://doi.org/10.1107/S0021889813003531

31. ASTM E8/E8M-22 (2022) Standard Test Methods for Tension Testing of Metallic Materials. https://doi.org/10.1520/E0008_E0008M-22

32. International Organization for Standardization (2023) ISO 5173:2023 Destructive tests on welds in metallic materials. Bend tests. https://www.iso.org/standard/81724.html. Accessed 4 Mar 2023

33. ASTM E112-13 (2021) Standard Test Methods for Determining Average Grain Size. https://doi.org/10.1520/E0112-13R21

34. Llovet X, Moy A, Pinard PT, Fournelle JH (2021) Reprint of: Electron probe microanalysis: A review of recent developments and applications in materials science and engineering. Prog Mater Sci 120:100818. https://doi.org/https://doi.org/10.1016/j.pmatsci.2021.100818

35. Portebois L, Mathieu S, Bouizi Y, et al (2014) Effect of boron addition on the oxidation resistance of silicide protective coatings: A focus on boron location in as-coated and oxidised coated niobium alloys. Surf Coat Technol 253:292–299. https://doi.org/https://doi.org/10.1016/j.surfcoat.2014.05.058

36. Di Luozzo N, Fontana M, Arcondo B (2008) Transient liquid phase bonding of steel using an Fe–B interlayer: microstructural analysis. J Mater Sci 43:4938–4944. https://doi.org/10.1007/s10853-008-2720-0

37. Kolmogorov AN, Shah S, Margine ER, et al (2010) New Superconducting and Semiconducting Fe-B Compounds Predicted with an Ab Initio Evolutionary Search. Phys Rev Lett 105:217003. https://doi.org/10.1103/PhysRevLett.105.217003

38. Taylor KA, Hansen SS (1990) The boron hardenability effect in thermomechanically processed, direct-quenched 0.2 Pct C steels. Metallurgical Transactions A 21:1697–1708. https://doi.org/10.1007/BF02672586

39. Hara T, Asahi H, Uemori R, Tamehiro H (2004) Role of Combined Addition of Niobium and Boron and of Molybdenum and Boron on Hardnenability in Low Carbon Steels. ISIJ International 44:1431–1440. https://doi.org/10.2355/isijinternational.44.1431

40. Drillet J, Valle N, Iung T (2012) Nanometric Scale Investigation of Phase Transformations in Advanced Steels for Automotive Application. Metallurgical and Materials Transactions A 43:4947–4956. https://doi.org/10.1007/s11661-012-1218-1

41. Da Rosa G, Maugis P, Portavoce A, et al (2020) Grain-boundary segregation of boron in high-strength steel studied by nano-SIMS and atom probe tomography. Acta Mater 182:226–234. https://doi.org/https://doi.org/10.1016/j.actamat.2019.10.029

42. Prithiv TS, Gault B, Li Y, et al (2023) Austenite grain boundary segregation and precipitation of boron in low-C steels and their role on the heterogeneous nucleation of ferrite. Acta Mater 252:118947. https://doi.org/https://doi.org/10.1016/j.actamat.2023.118947

43. Da Rosa G, Maugis P, Portavoce A, et al (2023) Boron segregation at austenite grain boundaries: An equilibrium phenomenon. Acta Mater 255:119098. https://doi.org/https://doi.org/10.1016/j.actamat.2023.119098

44. Fujishiro T, Hara T, Shigesato G (2015) Effect of Mo on γ to α Transformation and Precipitation Behavior in B-added Steel. Tetsu-to-Hagane 101:300–307. https://doi.org/10.2355/tetsutohagane.101.300

45. American Petroleum Institute (API) (2021) API STANDARD 1104Welding of Pipelines and Related Facilities 22nd Edition. American Petroleum Institute

46. SAE J1397_202403 (2024) Estimated Mechanical Properties and Machinability of Steel Bars. https://doi.org/https://doi.org/10.4271/J1397_202403